Influence of Low and Extreme Heat Fluxes on Thermal Degradation of Carbon Fibre-reinforced Polymers

Johannes Bibinger[1,2] · Sebastian Eibl[2] · Hans-Joachim Gudladt[1]

Abstract

This study considers the influence of different irradiation scenarios on the thermal degradation of carbon fibre-reinforced polymers (CFRP). Real threats are simulated, such as fires with long-lasting low heat fluxes and nuclear heat flashes with short-lasting high heat fluxes. For this purpose, coated and uncoated quasi-isotropic samples of the commercially available CFRP HexPly® 8552/IM7 are thermally irradiated from one side by an electrical heater of a cone calorimeter and a xenon short-arc lamp of a laboratory heat flash simulator with heat fluxes between 5 and 175 W/cm^2 at varying time intervals. The specimens' temperature is recorded on the front and back side as well as at different laminate depths. The CFRP are analyzed with ultrasonic testing (UT), infrared spectroscopy (ATR-FTIR), scanning electron microscopy (SEM) and micro-focused computed X-Ray tomography (µCT). Destructive tests are performed to determine the mechanical properties in terms of interlaminar shear, compressive and tensile strength. When samples of CFRP are exposed to higher heat flux, high temperatures and temperature gradient values occur along the crosssection. As a result, extreme damage gradients appear in the material, leading to changes in damage behavior and loss of mechanical properties within seconds. However, to ensure the safety of the material in case of thermal exposure, loading limits are introduced, indicating the threshold for strength collapse. In addition, with the application of coatings, thermal degradation of CFRP can be delayed. Finally, the time-heat flux superposition principle is established to predict the residual strength under different loading scenarios.

✉ Johannes Bibinger
  Johannes.Bibinger@unibw.de

1   University of the Bundeswehr Munich – Institute for Material Science, Werner-Heisenberg-Weg 39, 85579 Neubiberg, Germany

2   Fuels and Lubricants (WIWeB), Bundeswehr Research Institute for Materials, Institutsweg 1, 85435 Erding, Germany

1 Introduction

Carbon fibre-reinforced polymers (CFRP) are characterized by high strength and stiffness combined with low weight [1, 2]. Due to these properties, the composite materials are used especially in aerospace industry and shall replace light metals in aircraft construction as far as possible [3–5]. In contrast to metallic structures, CFRP have a very low thermal conductivity and resistance due to the polymer matrix [6–10]. To guarantee a safe application, it is necessary to know the mechanical and thermal properties as well as the degradation mechanism of the material in case of heat-induced damage. Since aircraft can be exposed to threats such as fully developed fires (heat flux $q \sim 5$ W/cm^2 [11]), burning fuels ($q \sim 15$ W/cm^2 [12]), burning propellants ($q \sim 20$ W/cm^2 [12]), warheads ($q \sim 50$ W/cm^2 [12]) or high-power laser ($q \sim 10^2 - 10^4$ W/cm^2 [13, 14]), different heat scenarios must be considered. In general, these scenarios may be classified into three groups:

– Low heat fluxes $q \leq 5$ W/cm^2 = Effect of fire progression
– Medium heat fluxes 5 W/cm$^2 < q < 50$ W/cm^2 = Effect of fire accelerant
– High heat fluxes $q \geq 50$ W/cm^2 = Effect of weapon systems

Characteristic for these thermal threats is the one-sided thermal loading of the composite material. In this case, radiation from the heat source impinges on the front side. Part of the radiation is reflected, emitted and absorbed by the surface [15]. Since no impinging irradiation energy is transmitted by the black CFRP, only the absorbed heat is conducted from the front to the back side. With rising heating, thermal, chemical and physical decomposition processes occur [16–18]. Thereby, a damage gradient along the material cross-section is formed which can be generally divided into fibre, fibre-char, decomposition reaction front and virgin material region, containing delamination, matrix cracking as well as fibre-matrix debonding [16–18]. However, the degradation processes and damage regions depend on the heat flux and can affect failure processes and mechanical properties differently.

Up to now, investigations on thermal degradation of CFRP with and without coating are mostly limited to low and medium heat fluxes or pre-loads in thermal equilibrium [19–24]. These thermal loads are characterized by slow material heating $\theta \leq 20$ °C/s or low constant exposure temperatures $T \leq 350$ °C [19–25]. In both cases, the decomposition of the individual components takes place slowly and temporally separated compared to high heat fluxes [19, 26]. For example, when CFRP with typical coating are heated, first the binder decomposes, causing color changes of the coating, and later at higher temperatures the epoxy resin [19, 20]. Thereby, the low thermal stability of the binder can be exploited by using the specific color changes as an early warning system for material damage [27].

At high heat fluxes, this indirect indication of thermal damage can only be used restrictively. In these scenarios, much more energy per time interval impinges on the surface, resulting in rapid heating $\theta \geq 200$ °C/s of the sample. Consequently, front side temperatures over $T > 1000$ °C arise within seconds, leading directly to decomposition processes and combustion of the material [14]. The irradiation scenarios thus vary in the heating rate, affecting the damage mechanism and distribution along the specimen cross-section unequally.

This work characterizes the one-sided thermal damage of the composite material HexPly® 8552/IM7 under different loading scenarios with focus on high heat fluxes. Real thermal threats like fires or nuclear heat flashes are simulated. Thereby, both the

coated and uncoated quasi-isotropic material is exposed either to long-lasting low heat fluxes ($q = 5$ W/cm^2 until $t_1 \leq 40$ s) with an electrical heater of a cone calorimeter or short-lasting high heat fluxes ($q = 50$, 110 and 175 W/cm^2 until $t_1 \leq 5$ s) with a xenon short-arc lamp of a laboratory heat flash simulator. During this process, the temperature is recorded at various laminate depths. Moreover, the thermally damaged samples are tested with non-destructive and destructive methods.

The aim of this study is to identify the influence of different loading scenarios on the thermal degradation of CFRP. Thus, the interaction between heat flux and exposure time in terms of temperature and damage distribution, degradation mechanism, mechanical properties and sensitivity of strength types are considered. To ensure the safety of the material in case of thermal irradiation, loading limits are introduced, representing the threshold for strength collapse. Furthermore, the protective effect of surface coatings on carbon fibre-reinforced polymers is analyzed. Finally, the mechanical properties are predicted under different loading scenarios.

2 Material

In this study, all investigations are performed on the commercially available CFRP HexPly® 8552/IM7 by Hexcel Composites GmbH. The unidirectional prepregs consist of 58 wt. % HexTow® IM7 carbon fibres which are pre-impregnated with the 8552 epoxy based resin system [28]. The polymer matrix is composed of the epoxy components tetraglycidyl methylene dianiline (TGMDA) and triglycidyl-p-aminophenol (TGPAP), the curing agent 3,3'- or 4,4'-diaminodiphenyl sulfone and the thermoplastic toughener polyethersulfone (PES) [29]. PES reduces the stiffness of the epoxy resin and increases the interlaminar shear strength of the material [29]. Sixteen prepreg plies with a nominal cured ply thickness of 0.131 mm are laminated to approximately 2 mm thick panels with $[(+45/90/\text{-}45/0)_2]_s$ quasi-isotropic lay-ups. Furthermore, type K thermocouples are laminated between 2/3, 6/7, 12/13 ply and attached on the front as well as back side with peel ply. The laminates are cured in an autoclave according to the manufacturer's recommended conditions [28]. A fibre volume content of 68 wt. % is achieved. Ultrasonic C-scans are performed to ensure material quality without macroscopic delaminations, pores and fibre orientation errors.

One part of the cured bulk material is coated with a 60 µm thick layer of the epoxy-based primer SEEVENAX® 113–24 and a 60 µm thick layer of the two-component polyurethane-based topcoat ALEXIT® 472–22, both from Mankiewicz GmbH [30, 31]. The grey color is typical for military aircraft FS 35,237 (Federal Standard 595C, Paint Spec) with semi-gloss. The laminates are cut with a water-cooled diamond wheel saw to $20 \times 10 \times 2$ mm^3 specimens for non-destructive and short beam shear tests, to $110 \times 10 \times 2$ mm^3 samples for compressive tests and to $250 \times 10 \times 2$ mm^3 specimens for tensile tests, respectively. For compressive and tensile strength tests, glass fibre tabs with $50 \times 10 \times 2$ mm^3 or $65 \times 10 \times 2$ mm^3 are applied at the end of both specimen sides using the universal two-component epoxy resin adhesive DELO-DUOPOX 1895 according to the manufacturer's recommended specifications [32]. Before thermal loading, all specimens are dried in a heating chamber with forced convection for one week at $T = 70$ °C.

Table 1 Summary of heat flux q, irradiation time t_I, heating rate θ on the front side, temperature difference ΔT between front and back side with hint of ignition state as well as residual interlaminar shear strength τ, compressive strength σ_c, tensile strength σ_t, stiffness E and damage behaviour of 8552/IM7 specimens with and without coating

q / W/cm²	t_I / s	θ / °C/s	ΔT / °C	8552/IM7				8552/IM7 + coat			
				τ / MPa	σ_c / MPa	σ_t / MPa	E / GPa	τ / MPa	σ_c / MPa	σ_t / MPa	E / GPa
0	0	0	0	71^{s}	746^{cf}	890^{c}	60^{c}	69^{s}	714^{cf}	903^{c}	57^{c}
5	5	14	16	68^{s}	728^{cf}	908^{c}	61^{c}	69^{s}	717^{cf}	902^{c}	55^{c}
	10	12	16	65^{s}	764^{cf}	900^{c}	59^{c}	66^{s}	724^{cf}	896^{c}	54^{c}
	15	11	17	64^{s}	742^{cf}	892^{c}	61^{c}	66^{s}	730^{cf}	913^{c}	56^{c}
	20	11	18	36^{s}	676^{cf}	889^{c}	60^{c}	52^{s}	721^{cf}	911^{c}	58^{c}
	25	11	23	26^{ns}	680^{cf}	835^{c}	59^{c}	24^{ns}	664^{cf}	848^{c}	54^{c}
	30	10	51	14^{ns}	654^{cf}	810^{c}	58^{c}	22^{ns}	584^{cf}	791^{c}	53^{c}
	35	10	82	4^{ns}	420^{cf}	821^{c}	57^{c}	13^{ns}	351^{cf}	781^{b}	55^{c}
	40	10	104	2^{ns}	-	570^{b}	47^{b}	-	-	725^{b}	51^{b}
50	0.5	328	105	68^{s}	746^{cf}	921^{c}	60^{c}	71^{s}	723^{cf}	898^{c}	54^{c}
	1.0	264	263	71^{s}	670^{cf}	892^{c}	60^{c}	69^{s}	706^{cf}	863^{c}	55^{c}
	1.5	233	327	73^{s}	721^{cf}	942^{c}	61^{c}	67^{s}	695^{cf}	853^{c}	51^{c}
	2.0	213	424	65^{s}	610^{blcf}	915^{c}	58^{c}	66^{s}	730^{cf}	877^{c}	54^{c}
	2.5	199	443	59^{s}	590^{cf}	876^{blc}	57^{blc}	67^{s}	709^{cf}	860^{c}	55^{c}
	3.0	188	552	55^{s}	522^{blcf}	844^{blc}	55^{blc}	68^{s}	685^{cf}	884^{c}	54^{c}
	4.0	172	828^{i}	45^{s}	496^{blcf}	783^{blc}	49^{blc}	61^{s}	610^{cf}	927^{c}	58^{c}
	5.0	160	820^{i}	18^{ns}	446^{blcf}	597^{blc}	48^{blc}	52^{s}	579^{cf}	925^{c}	57^{c}

Table 1 (continued)

q / W/cm²	t_i / s	θ / °C/s	ΔT / °C	8552/IM7 τ / MPa	σ_c / MPa	σ_t / MPa	E / GPa	8552/IM7+coat τ / MPa	σ_c / MPa	σ_t / MPa	E / GPa
110	0.3	617	199	66[s]	629[cf]	901[c]	62[c]	72[s]	704[cf]	826[c]	53[c]
	0.5	431	398	70[s]	683[blcf]	905[c]	60[c]	65[s]	688[cf]	894[c]	56[c]
	0.8	349	410	63[s]	531[blcf]	899[blc]	58[blc]	65[s]	740[cf]	909[c]	55[c]
	1.0	300	421	62[s]	565[blcf]	871[blc]	56[blc]	68[s]	682[cf]	873[c]	54[c]
	1.5	243	504[i]	59[s]	606[blcf]	885[blc]	55[blc]	69[s]	723[cf]	936[c]	56[c]
	2.0	209	619[i]	56[s]	564[blcf]	857[blc]	55[blc]	63[s]	638[cf]	899[c]	56[c]
	2.5	186	719[i]	38[s]	521[blcf]	776[blc]	52[blc]	57[s]	610[cf]	929[c]	57[c]
	3.0	170	784[i]	15[ns]	500[blcf]	707[blc]	52[blc]	49[s]	588[cf]	931[c]	58[c]
175	0.1	1496	75	71[s]	631[cf]	890[c]	60[c]	71[s]	704[cf]	873[c]	57[c]
	0.3	848	188	68[s]	678[blcf]	876[c]	61[c]	69[s]	726[cf]	850[c]	56[c]
	0.5	552	377	69[s]	568[blcf]	921[blc]	60[blc]	66[s]	689[cf]	840[c]	56[c]
	0.8	430	539[i]	60[s]	582[blcf]	921[blc]	60[blc]	67[s]	711[cf]	864[c]	56[c]
	1.0	360	701[i]	62[s]	619[cf]	900[blc]	59[blc]	61[s]	672[cf]	862[c]	56[c]
	1.3	313	863[i]	52[s]	500[blcf]	864[blc]	59[blc]	64[s]	626[cf]	867[c]	57[c]
	1.5	280	1025[i]	56[s]	595[blcf]	828[blc]	54[blc]	61[s]	694[cf]	869[c]	56[c]
	1.8	254	1025[i]	42[s]	500[blcf]	859[blc]	57[blc]	62[s]	630[cf]	858[c]	57[c]
	2.0	234	1024[i]	31[s]	427[blcf]	786[blc]	54[blc]	58[s]	632[cf]	900[blc]	61[blc]
	2.5	204	1024[i]	13[ns]	439[blcf]	779[blc]	51[blc]	48[s]	541[cf]	818[blc]	56[blc]
	3.0	182	1017[i]	4[ns]	350[blcf]	568[blc]	48[blc]	23[ns]	527[blcf]	835[blc]	56[blc]

i ignition, *s* shear, *ns* no shear, *cf* compressive failure, *c* crack, *b* brooming

3 Experimental

3.1 Thermal Treatment and Detection

Thermal irradiations at $q = 5$ W/cm^2 are performed with the electrical conical heater of a cone calorimeter from Fire Testing Technology up to a loading time of $t_l = 40$ s [33]. The entire sample front side is exposed to the homogeneous radiation. With a xenon short-arc lamp of a laboratory heat flash simulator from Siemens GmbH, heat fluxes of $q = 50$, 110 and 175 W/cm^2 up to an irradiation time of $t_l = 5$ s are generated. The generated beams are focused on a circular area in the center of the specimen, following a Gaussian intensity distribution [34]. The spectral intensity distribution corresponds approximately to a black body at a temperature of $T = 6000$ K and is therefore similar to the sunlight [34, 35]. An overview of irradiation conditions like heat flux q, irradiation time t_l and heating rate θ on the front side is shown in Table 1.

On the front side, the temperature is recorded with the infrared camera VarioCam® high resolution from InfraTec in a measuring range of $T_{meas} = -40 – 1200$ °C with an accuracy of $\pm 2\%$ (see Fig. 1(a)) [36]. The maximum surface temperatures are determined with the help of the recorded thermograms (see Table 2). The temperature on the surface and in different sample depths is measured with attached and laminated type K thermocouples in a measuring range of $T_{meas} = -180 – 1200$ °C with an accuracy of $\pm 0.4\%$ using the USB TC-08 data logger from pico Technology (see Fig. 1(b)) [37, 38]. Temperatures up to approximately $T \sim 1300$ °C can still be measured with both measuring techniques, considering that the measurement uncertainty increases.
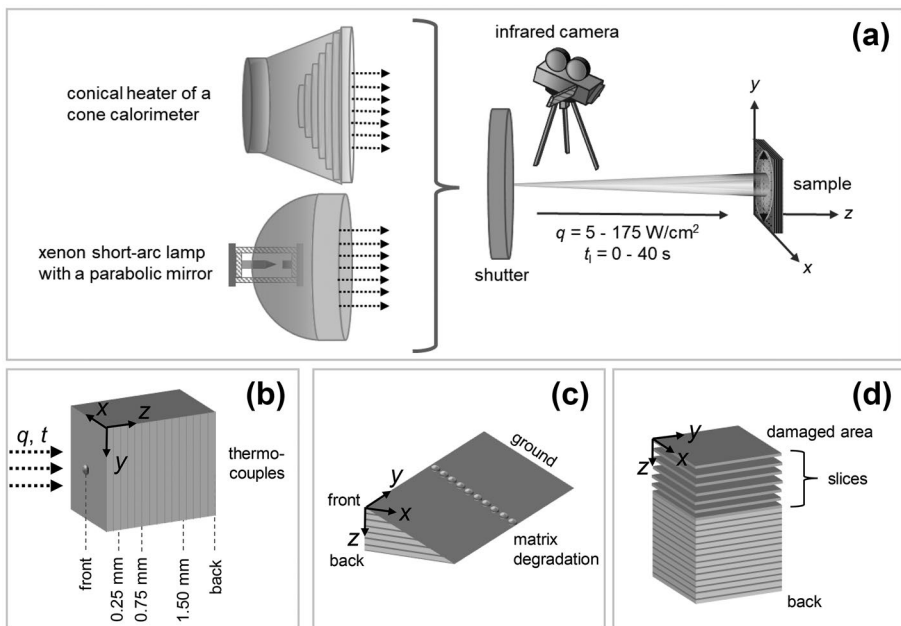

Fig. 1 Schematic overview of **a** irradiation experiments and depth-dependent measurements of **b** temperature using thermocouples, **c** matrix degradation using infrared spectroscopy as well as **d** damaged area using micro-focused computed X-Ray tomography

Table 2 Qualitative comparison of (a) photos, (b) ultrasonic C-scans, (c) μCT sectional images in x–y-plane at a sample depth of $z = 0.06$ mm and (d) thermal images of the front side for different irradiation scenarios. Additionally, the temperature rises T_r^f on the front side, the attenuated area δ_d/δ_0 of the ultrasonic signal, the damaged area A_d/A_0 of the μCT signal as well as the temperature T over the entire specimen front side are given

t_i / s	$q = 5$ W/cm² 8552/IM7 T_r^f /°C (a₁)	δ_d/δ_0 /% (b₁)	A_d/A_0 /% (c₁)	T /°C (d₁)	8552/IM7 + coat T_r^f /°C (a₂)	δ_d/δ_0 /% (b₂)	A_d/A_0 /% (c₂)	T /°C (d₂)	t_i / s	$q = 175$ W/cm² 8552/IM7 T_r^f /°C (a₃)	δ_d/δ_0 /% (b₃)	A_d/A_0 /% (c₃)	T /°C (d₃)	8552/IM7 + coat T_r^f /°C (a₄)	δ_d/δ_0 /% (b₄)	A_d/A_0 /% (c₄)	T /°C (d₄)
0	0	0	0	0	0	0	0	0	0	0	0	0	0	0	0	0	0
5	90	0	0	65	94	0	0	66	0.10	455	22	5	378	535	66	0	391
10	179	0	0	168	176	0	0	175	0.25	630	65	7	415	669	100	0	414
15	241	0	0	222	245	0	0	224	0.50	694	99	32	452	1000	100	0	552
20	297	0	4	264	298	0	0.1	260	0.75	779	100	49	646	1072	100	0.1	651
25	351	100	18	306	340	100	0.5	300	1.25	963	100	45	855	1233	100	6	861
40	506	100	44	-	505	100	52	-	2.00	1336	100	47	1269	1399	100	32	1072

Color scale δ / dB: -50, -40, -30, -20, -10, 0
Color scale T / °C: 1400, 1100, 800, 600, 300, 0

To determine the emissivity ε of the impinging radiation, coated and uncoated 8552/IM7 specimens are heated up to $T \sim 200$ °C with a hot plate and the temperature is simultaneously recorded with attached thermocouples and infrared camera [36]. Since identical temperatures are measured, no adjustment of the emission input of the camera is necessary. The result is an emission coefficient of $\varepsilon = 1.0$ according to Kirchhoff's law [39].

3.2 Non-Destructive Testing

The matrix degradation and oxidation of the composite material can be quantified by micro attenuated total reflection Fourier transform infrared spectroscopy (ATR-FTIR). To examine the sample surface, spectra are recorded with 32 scans in a range of $\tilde{v} = 4000 - 400$ cm^{-1} using a Bruker Tensor 27 spectrometer equipped with a Harrick ATR cell and a silicon crystal. In addition, the $20 \times 10 \times 2$ mm³ specimens are ground with an angle of 11° along the specimen width to determine matrix degradation in different depths (see Fig. 1(c)). The spectra are recorded in a step size of 0.06 mm with 100 scans in identical range using the thermoelectric detector and germanium crystal of LUMOS II from Bruker.

With the scanning electron microscope (SEM) Ultra Plus from Zeiss, the topography of the thermal damage in the specimen center is recorded. A voltage of 1.0 kV is applied and the resulting image of the secondary electrons is evaluated.

Using General Electric's micro-focused computed X-Ray tomography V-TOME XL 300 system with a 180 kV source, volumes are recorded in a $10 \times 10 \times 2$ mm³ section from the sample center and sliced into 32 x–y-planes with a voxel size of 10 μm (see Fig. 1(d)). In these tomograms, defects such as delaminations and cracks can be detected, since X-rays

are less absorbed by air or pyrolysis gases compared to bulk material like CFRP, resulting in darker voxels [40]. The voxels can be investigated in the RGB color model (R = red, G = green and B = blue), where black corresponds to (0, 0, 0) and white to (255, 255, 255). By means of a gray scale analysis, the damaged area is quantified by defining the lowest RGB voxel values for thermally undamaged sample as threshold. RGB values below this threshold are counted as voxels, representing damaged CFRP material. The percentage damaged area A_d/A_0 is the ratio between these and the total number of voxels in the tomogram.

Ultrasonic C-scans are recorded with the Hill-Scan 3060 UHF from Dr. Hillger according to DIN EN ISO 16810 [41]. The test head Panametrics 20 MHz is used with a frequency of 15 MHz and a step width of 0.1 mm. The damaged area can be detected via the auxiliary reflector signal and quantified with a gray scale analysis similar to micro-focused computed X-Ray tomography.

The glass transition temperature T_g of the material is determined by the dynamic mechanical analysis DMA GABO EPLEXOR® from Netzsch. The loss modulus E'' is measured depending on the temperature at three-point bending loading of a $60 \times 10 \times 2$ mm^3 sample with a frequency of 1 Hz.

3.3 Destructive Testing

The carbon fibres IM7 and the extracted epoxy resin as well as thermoplastic polyether-sulfone are examined with the thermogravimetric analyzer TG 209 F1 from Netzsch. The components are heated up to $T = 1000$ °C at a heating rate of 10 K/min under air atmosphere. The beginning of thermal component decomposition is determined via the onset temperature.

Interlaminar shear strength (ILSS) of CFRP is determined with the short beam shear test at a constant rate of 1 mm/min on the universal testing machine Zwick/Roell Z020 according to DIN EN 2563 [42]. During the measurement, the samples rest with the front side on the two lower supports. Tensile strength of the material is tested at a constant rate of 2 mm/min with a Zwick/Roell Z250 in accordance to DIN EN ISO 527–4 [43]. The Zwick/Roell multiXtens extensometer and the force transducer Xforce K measure the elongation of the sample and applied force. The material stiffness during tensile test is calculated for all specimens in a strain range of 0.05 and 0.25%. Compressive strength is determined with the testing machine Zwick/Roell Zmart.pro 1485 at a constant rate of 1 mm/min according to DIN EN ISO 14126 [44]. The applied force is measured with the load sensor Zwick/Roell Z12.

4 Results and Discussion

4.1 Temperature Distribution

When carbon fibre-reinforced polymers are thermally loaded from one side, the irradiation energy impinges on the front side of the specimen. Thereby, part of this radiation is emitted, reflected or absorbed by the surface [15]. Only the absorbed energy is conducted from the front to the back side, resulting in heating of the material. To illustrate this, Fig. 2 shows temperature profiles during heating (solid lines) and cooling (dotted lines) in different sample depths z at (a) $q_1 = 5$ W/cm^2, (b) $q_2 = 50$ W/cm^2, (c) $q_3 = 110$ W/cm^2 and (d)
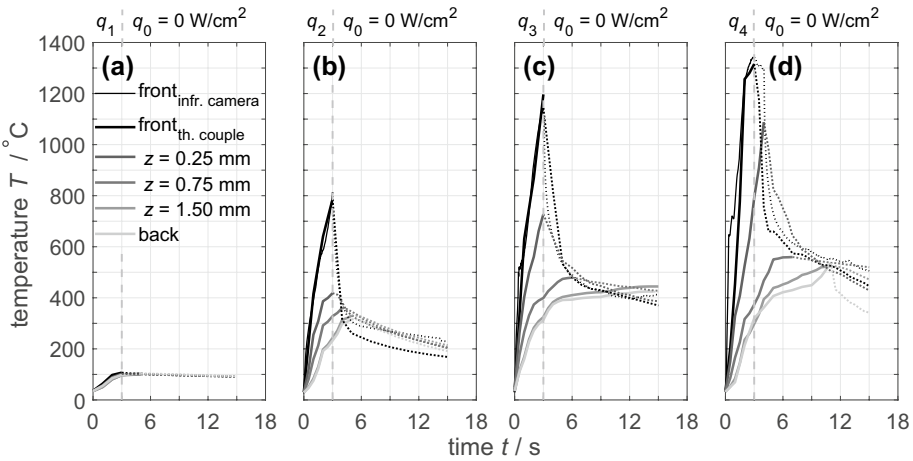
Fig. 2 Temperature profiles at **a** $q_1 = 5$ W/cm^2, **b** $q_2 = 50$ W/cm^2, **c** $q_3 = 110$ W/cm^2 and **d** $q_4 = 175$ W/cm^2 for an irradiation over 3 s in different laminate depths z. The heating process is visualized with continuous lines and the cooling process ($q_0 = 0$ W/cm^2) with dotted lines

$q_4 = 175$ W/cm^2 for a constant irradiation time of $t_1 = 3$ s. During thermal irradiation, the front side heats up faster with rising heat flux. Thereby, the front side temperature can be measured with attached thermocouples (thick black line) as well as infrared camera (thin black line). Up to $T \sim 1300$ °C, the measured temperatures of both methods correspond well. At the longest exposure time, the temperatures deviate by only $\Delta T / T_{max} \leq 4\%$ compared to the maximum temperature. The slope of these $T(t)$-curves represents the heating rate. Accordingly, heating rates on the front side of $\theta = \partial T / \partial t = 18$ and 360 °C/s set in at $q = 5$ and 175 W/cm^2 within $t_1 = 1$ s. With rising exposure time and sample depth, the heating rate declines, resulting in slower material heating (see also Table 1). As soon as no more irradiation energy impinges on the sample surface $t > t_1$, the heat is still propagating in the specimen, leading to heating in deeper plies [25, 45]. For example, at the highest heat flux of $q = 175$ W/cm^2, the back side temperature rises to $T_b = 335$ °C in $t_1 = 3$ s. During cooling of $t = 8$ s, a maximum back side temperature of $T_b = 536$ °C and a temperature difference between front and back side of $\Delta T = 10$ °C is reached. Thus, the equalization of the temperature along the cross-section leads to a heating of the back side by 201 °C after thermal irradiation. In contrast, at the lowest heat flux of $q = 5$ W/cm^2, the equalization leads to a maximum back side temperature rise of only 5 °C due to the lower temperature difference.

Furthermore, Fig. 3 shows the temperature rise T_r as a function of the sample depth z at (a) $q = 5$ W/cm^2 and (b) $q = 175$ W/cm^2. The progression of the temperature gradient is visualized by the temperature-depth $T(z)$-curves. At the lowest heat fluxes, only small temperature differences occur between the front ($z = 0$ mm) and back ($z = 2$ mm) side. For example, a temperature difference of only $\Delta T = 23$ °C appears in $t_1 = 25$ s. With rising heat flux and exposure time, the temperature gradient increases. At the highest heat fluxes, temperature differences of $\Delta T = 701$ and 1023 °C are reached in $t_1 = 1$ and 2.5 s, respectively. Consequently, during thermal loading with high heat fluxes, enormous radiation energies per time interval impinge on the surface. As a result, the material heats up rapidly, leading to the formation of an extreme temperature gradient. After irradiation, the temperature gradient equalizes, causing continued heating and thermo-induced damage in deeper plies.
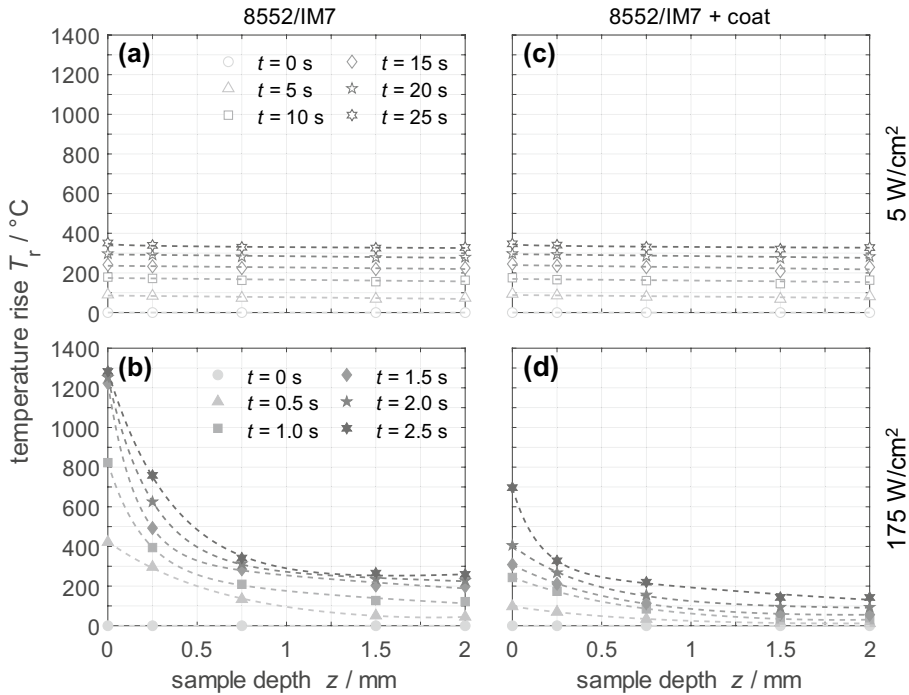
Fig. 3 Temperature gradients between front ($z=0$ mm) and back ($z=2$ mm) side at heat fluxes of $q=5$ and 175 W/cm² for **a**, **b** 8552/IM7 and **c**, **d** 8552/IM7 with coating

4.2 Mechanism of Thermal Material Degradation

The thermal decomposition of carbon fibre-reinforced polymers depends on factors such as heating rate and surface of the material [26]. In thermogravimetric analyses with constant heating rate of $\theta=10$ °C/min ($\theta=0.17$ °C/s), decomposition under oxygen atmosphere starts for 8552 epoxy resin at an onset temperature of $T_{0,\text{ep}}=270$ °C, for polyethersulfone at $T_{0,\text{pes}}=510$ °C and for IM7 fibres at $T_{0,\text{cf}}=608$ °C in powder form. With rising heating rate, the onset temperatures shift to higher temperatures [26]. This shift occurs due to the delay between measured temperature and effective temperature in the sample as well as the lower exposure time at each temperature, resulting in lower amount of decomposition products at each temperature. Thus, for the one-sided thermally loaded samples, both lower surfaces due to the compact material and higher heating rates compared to the thermogravimetric analyses are present, resulting in no significant decomposition of the components below the specified onset temperature.

Matrix degradation can be characterized and quantified by ATR-FTIR spectroscopy due to the different thermal stabilities of the epoxy resin and the polyethersulfone [25, 29]. For illustrative purposes, Fig. 4 shows infrared spectra (a) on the front side at different exposure times and (b) in different depths at constant exposure time. With increasing thermal loading of the samples, the C=O stretching vibration intensity between 1630 and 1790 cm⁻¹ increases due to the oxidation products on the surface [46, 47]. In contrast, the band intensity at 1510 and 1600 cm⁻¹, assigned to the C–C stretching vibration of the
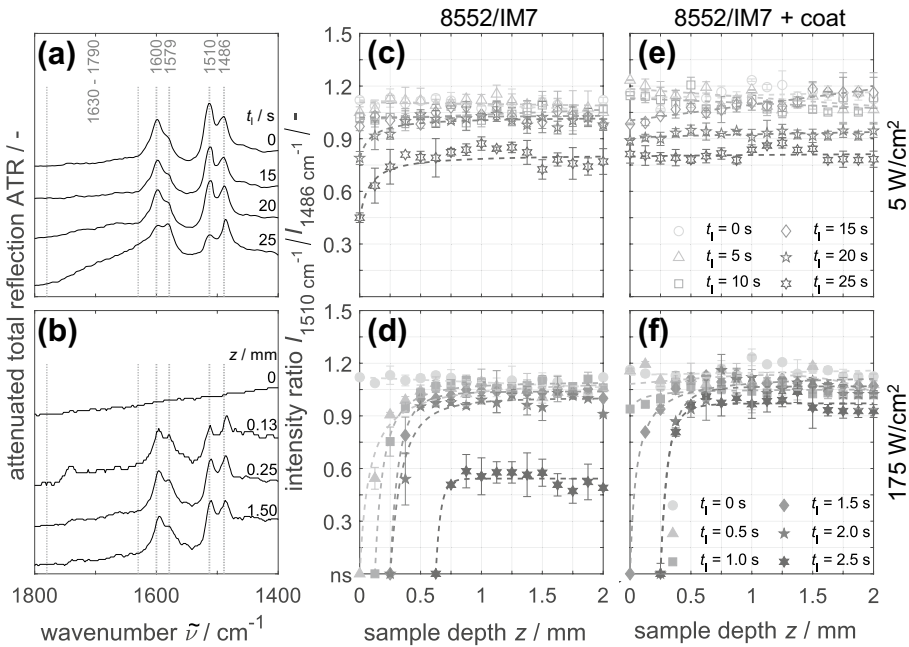
Fig. 4 ATR-FTIR spectra of 8552/IM7 at **a** $q = 5$ W/cm^2 and varying exposure time t_l on the front side as well as **b** $q = 175$ W/cm^2 and varying sample depth z after $t_l = 2.0$ s. In addition, the intensity ratio $I_{1510 \text{ cm}^{-1}}/I_{1486 \text{ cm}^{-1}}$ at $q = 5$ and 175 W/cm^2 for **c, d** 8552/IM7 and **e, f** 8552/IM7 with coating are shown

aromatic ring structure in the epoxy resin, decrease [46, 47]. Whereas the intensity of the bands at 1486 and 1579 cm^{-1}, assigned to the analogue vibration of the polyethersulfone, remains constant [24, 48]. The spectra visualize the preferred thermal decomposition progress of the epoxy resin, which can be quantified by the intensity ratio of the bands at 1510 and 1486 cm^{-1}. This band intensity ratio is 1.12 ± 0.02 in initial state and drops with rising thermal exposure and declining sample depth until finally no signal can be detected.

Furthermore, Fig. 4 shows the intensity ratio $I_{1510 \text{ cm}^{-1}}/I_{1486 \text{ cm}^{-1}}$ depending on the sample depth z at (c) $q = 5$ W/cm^2 and (d) $q = 175$ W/cm^2. At the lowest heat flux, no significant matrix degradation is visible until $t_l \leq 10$ s. Up to this exposure time, the 8552/IM7 glass transition temperature of $T_g = 229$ °C is not exceeded. However, a slight mass increase of $\Delta m/m_0 = 0.4\%$ appears, indicating the formation of oxidation products and thus a thermo-oxidative damage near the surface. With continued thermal irradiation, the infrared intensity ratio drops continuously over the cross-section, resulting in moderate matrix degradation and weakening of the fibre-matrix bonding. From $t_l \geq 20$ s, matrix degradation is more pronounced towards the front side. In contrast, at the highest heat flux no infrared signal can be detected on the front side after $t_l = 0.5$ s. Obviously, the matrix is already decomposed, confirmed by the mass loss of $\Delta m/m_0 = 0.5\%$. With rising sample depth, the intensity returns abruptly to the initial level. Similarly for longer exposure times, only the sample depth where no intensity of molecular vibrations is measured increases and the depth from the initial level decreases, until from $t_l = 2.5$ s this level also drops. Consequently, when carbon fibre-reinforced polymers are exposed to one-sided thermal stress, significant matrix degradation starts at temperatures of $T > T_g$. Since the material is heated

slowly at low heat fluxes, thermo-oxidative damage near the surface and thermal decomposition of the matrix occurs only at higher exposure times under the formation of small damage gradients. At high heat fluxes, matrix degradation occurs immediately and extremely pronounced to the front side. Thereby, a damage gradient is formed with a matrix depleted region, transition region and virgin region along the cross-section until ultimately the entire specimen is degraded.

Moreover, the thermal degradation on the composite surface is visualized in Table 3 using scanning electron micrographs at (a – d) $q = 5$ W/cm^2 (e – h) $q = 175$ W/cm^2 for different exposure times. At the lowest heat flux, a porous matrix structure as well as fibres become visible for $t_1 = 20$ s. Thereby, the intensity ratio drops to $I_{1510\ \text{cm}^{-1}}/I_{1486\ \text{cm}^{-1}} = 0.79$. Within $t_1 = 35$ s, the carbon fibres are only covered with a thin polymer film ($d \sim 0.6$ μm), which cannot be detected by ATR-FTIR spectroscopy. Investigations with SEM–EDX show that the thin film is composed of the elements carbon, sulfur, oxygen and nitrogen. The film likely consists of mainly molten polyethersulfone. For $t_1 = 105$ s, the matrix film is completely removed and the surface structure of the bare fibres are visible [49]. Now the fibres ($d = 5.2 \pm 0.2$ μm [50]) are directly exposed to thermal irradiation, but are not affected as long as the onset temperature $T_{0,\text{cf}} = 608$ °C is not reached. In comparison, previous experiments show that temperatures of approximately $T \sim 750$ °C ($q = 6$ W/cm^2) are applied over a time period of $t_1 = 20$ min, a reduction of the fibre diameter occurs over the entire length [51]. In contrast, at the highest heat flux, matrix depletion starts already in $t_1 = 0.5$ s. With rising thermal loading, the material ignites, leading to the formation of soot on the surface in $t_1 = 1.0$ s (see summary of all ignited samples in Table 1). Soot indicates the decomposition of carbon-containing compounds, which are mainly formed during combustion processes [52]. From $t_1 = 3.0$ s and a surface temperature of $T_r^f = 1355 \pm 40$ °C, decomposition of the molten polymer film sets in primarily, but also decomposition of the fibre itself in a few spots. Thus, at low heat fluxes, carbon fibre decomposition starts only after advanced exposure times, provided that the decomposition temperature is exceeded. In contrast, at high heat fluxes, this temperature is reached immediately on the front side, causing ignition of the sample and decomposition of fibres in few seconds.

In Fig. 5, micro focused X-ray tomograms are displayed in x–z as well as x–y planes to visualize the structural damage along the sample cross-section and ply plane at (a) $q = 5$ W/cm^2 and $t_1 = 20$ s as well as (b) $q = 175$ W/cm^2 and $t_1 = 2.0$ s. Defects such as delaminations, cracks and pores can be detected because X-rays are less absorbed by pyrolysis gases and

Table 3 Scanning electron micrographs of the specimens' front side for long-lasting low and short-lasting high heat fluxes
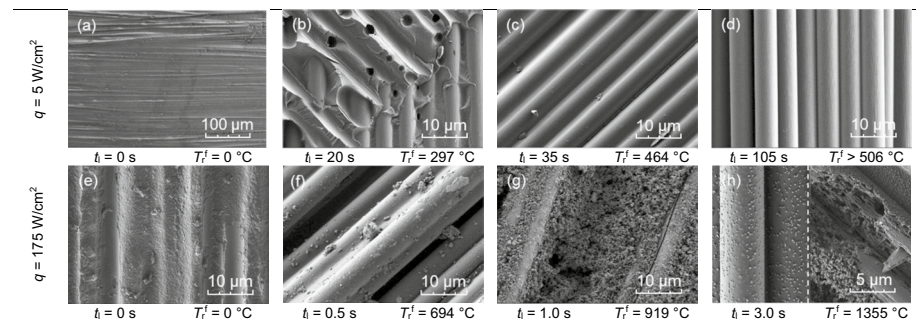
air compared to carbon fibre-reinforced polymer, resulting in darker voxels [40]. At the lowest heat flux, visible delaminations extend over the entire cross-section after $t_1 = 20$ s. Thereby, the delaminations occur in fibre direction of the quasiisotropic lay-up. For example, in a specimen depth of $z = 0.25$ mm delaminations are aligned in 90° direction and of $z = 0.78$ mm in –45° direction. In contrast, at the highest heat flux, an extreme damage distribution occurs where the region with matrix depletion and regions with and without structural damage become visible [16–18].

With the help of gray scale analysis and the introduction of a threshold value for undamaged material, the percentage damage in x–y plane can be determined. For this purpose, the damaged area A_d/A_0 is shown versus the sample depth z at (c) $q = 5$ W/cm^2 and (d) $q = 175$ W/cm^2 for different exposure times. At the lowest heat flux, no structural damage can be detected up to $t_1 \leq 15$ s. Only with rising thermal loading visible delaminations extend over the entire specimen cross-section under formation a small damage gradient. From $t_1 \geq 25$ s, the damage increases significantly in all depths. Since at this exposure time the decomposition temperature of the epoxy resin is far exceeded, pyrolysis gases can be produced which accumulate between the delaminations. Side effects are thermal expansion in z-direction and attenuation of the ultrasonic signal (see Table 3 (b_1)). Thereby, the large-area damage in x–y plane reduces the adhesion between the plies and hinders the heat conduction to the back side. As a result, the temperature rises much more on the front than on the back side, which is the explanation for the significant increase of the temperature gradient with time. In contrast, at high heat fluxes, the formation of defects starts within a few milliseconds due to the high heating rate. For example, after $t_1 = 0.5$ s delaminations already extend to a depth of $z = 0.3$ mm and reach a maximum damaged area of
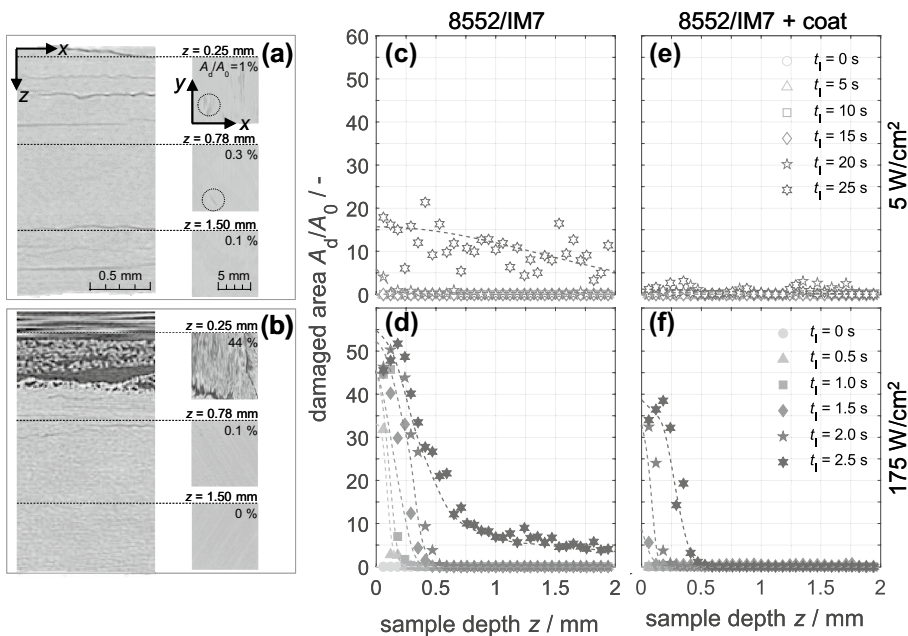

Fig. 5 Micro-focused computed X-Ray tomograms of 8552/IM7 **a** at $q = 5$ W/cm^2 and $t_1 = 20$ s as well as **b** at $q = 175$ W/cm^2 and $t_1 = 2.0$ s. In addition, the damaged areas A_d/A_0 at $q = 5$ and 175 W/cm^2 are visualized for **c**, **d** 8552/IM7 and **e**, **f** 8552/IM7 with coating

approximately $A_d/A_0 \sim 32\%$ near the front side. With rising exposure time, the maximum delamination depth and especially the damaged area towards the front side increases further. An extreme damage gradient occurs, where ply-by-ply over a large area $A_d/A_0 \sim 50\%$ is damaged. As a result, the sample thickness increases and the heat transport is significantly hindered. Consequently, during thermal loading with low heat fluxes, low heating rates and thus small damage gradients occur at higher exposure times. In contrast, at high heat fluxes, enormous heating rates occur, resulting in immediate decomposition processes and pronounced stresses along the specimen cross-section. As a result, defects near the surface are formed directly with the beginning of the irradiation (see defects in Table 3 ($a_3 - c_3$) for $t_1 = 0.1$ s). With rising heating, the number and area of damage increases extremely towards the front side.

In summary, during thermal loading with low heat fluxes, the material heats up slowly. As a result, low temperatures and temperature gradients occur, resulting in relatively small damage gradients along the sample cross-section. Thereby, the thermal degradation begins with matrix oxidation near the surface, weakening of the fibre-matrix bonding, pronounced matrix degradation, formation of delaminations, resin depletion and finally the decomposition of the fibres when the temperature is sufficiently high. In contrast, at high heat fluxes, much more irradiation energy per time interval impinges on the sample surface, leading to extreme material heating. As a result, the thermal degradation processes occur very early and almost simultaneously. Due to the high temperatures, the material combusts, causing extreme inhomogeneous thermal damage along the composite cross-section.

4.3 Influence of a Surface Coating

Surface coatings can affect the thermal degradation of carbon fibre-reinforced polymers. For this purpose, Fig. 3 visualizes temperature curves for coated samples at (c) $q = 5$ W/cm^2 and (d) $q = 175$ W/cm^2 next to the uncoated specimens. When coated specimens are thermally irradiated, the radiation energy impinges on the coating. Part of this radiation is reflected, emitted and absorbed by the coating. Subsequently, the absorbed heat is conducted from the coating into the sample. Thereby, the temperature differences between coated and uncoated specimen are negligible at low and significant at high heat fluxes. At low heat fluxes, similar temperatures are reached because the material is heated moderately and the coating only slightly increases the specific heat capacity. In contrast, at high heat fluxes, significantly lower temperatures are detected for the coated material. On the one hand, this effect is due to the coating thickness. The coating absorbs the extreme impinging energy and is thus exposed to very high temperatures near the surface, leading to significant reduction of the temperature gradient in the underlying sample. On the other hand, this effect is due to the white silicate filler in the top coat, identified by infrared spectroscopy [20]. Thermogravimetric analyses show that at $\theta = 10$ °C/min ($\theta = 0.17$ °C/s) thermal decomposition of the top coat begins from an onset temperature of $T_{0,c} \sim 275$ °C under oxygen atmosphere, whereas the silicate filler is thermally stable below $T < 1000$ °C. Thus, at high heat fluxes, the coating decomposes within a short exposure time and the thermally stable silicate filler remains on the surface. Thereby, the surface color changes from gray to white, leading to increased reflection of the impinging radiation (see Table 3 (a_4)). As a result, less energy is absorbed and the material heats up slower.

Figure 4 shows the intensity ratio $I_{1510 \text{ cm}^{-1}}/I_{1486 \text{ cm}^{-1}}$ determined by ATR-FTIR for the coated 8552 at (e) $q = 5$ W/cm^2 and (f) $q = 175$ W/cm^2 alongside the uncoated material. At the lowest heat flux, the matrix degradation of the 8552/IM7 with and without coating

hardly differs. In contrast, at the highest heat flux, matrix degradation is significantly less pronounced in coated specimens. For example, no infrared signal can be detected in $z = 0$ mm after $t_l \geq 0.5$ s for uncoated and only after $t_l \geq 1.5$ s for coated specimens. Thus, matrix degradation in this depth can be delayed by a temporal factor of $s_f = 1.5$ s / 0.5 s $= 3$.

Furthermore, Fig. 5 illustrates the damaged area A_d/A_0 determined by micro-focused computed X-Ray tomography of the coated specimens at (e) $q = 5$ W/cm^2 and (f) $q = 175$ W/cm^2 next to the uncoated material. Under identical irradiation conditions, both the maximum delamination depth as well as the damaged area are less pronounced in coated samples. In addition, the formation of delaminations can be significantly delayed at high heat fluxes. For example, at the highest heat flux, defects can be detected already after $t_l \geq 0.1$ s in uncoated samples and only after $t_l \geq 0.75$ s in coated samples (see also Table 3 (c$_3$)). Consequently, delamination formation is delayed by a factor of $s_f = 7.5$ for coated specimens, due to the reduced absorption of impinging radiation as well as the lower temperatures and thus stresses along the cross-section.

During moderate heating, the color of the coating can be changed by degradation of the binder. This color change can be detected with the spectrophotometry via the L*a*b* (L* = lightness, a* = red-green axis and b* = yellow-blue axis) values. With rising exposure time, the color of the coating changes from gray to a dark brown, resulting in a drop of L* and rise of a* and b* values [19, 20]. Since the L*a*b* values correlate with residual strength, the color change can be used to characterize thermal damage of the underlying composite material. However, the color change of the coating is only well resolved in time at low heat fluxes or in thermal equilibrium at low temperatures $T \leq 350$ [19, 20]. At high heat fluxes, the decomposition of the coating occurs starts very early, making the prediction of residual strength less meaningful. However, the white thermally stable silicate filler still remains on the surface, resulting in a pronounced reflection of the impinging radiation and thus protection of the carbon fibre-reinforced polymer.

4.4 Mechanical Properties

When carbon fibre-reinforced polymers are mechanically loaded, the influence of thermo-induced damage to mechanical properties can be characterized [20, 25, 53]. In the short bending test, the resistance parallel to the laminate plane is determined, providing information about the fibre-matrix adhesion [54]. In the compressive test, forces are applied via shear. As a result, one-sided thermally loaded specimens can be exposed to compressive, shear and bending stresses [44, 55]. Thereby, with decreasing fibre-matrix adhesion, fracture no longer occurs due to shear fracture but delamination [56]. In the tensile test, the force is transmitted by shear stress from fibres to matrix. When tensile stress is applied in fibre direction, the fibre strength dominates the composite strength [54]. Since the fibres are thermally very stable, the tensile strength is not very sensitive to the loading scenarios.

In the following, the occurring failure modes are described. When carbon fibre-reinforced polymers are heated, the failure phenomenon can change from shear failure in one or more plies to no shear failure in the interlaminar shear test. If no shear failure appears, the interlaminar shear strength is used solely as an indication of the residual strength [56]. Furthermore, when specimens are exposed to rising heat flux, the damage behavior can change from compressive failure to a combination with brooming during the compressive test (see Fig. 6 (c and d)) [54]. Brooming occurs when matrix depletion and thus extreme weakening of fibre-matrix adhesion are present. Thereby, the fibres are no longer embedded in the matrix. Similarly, during tensile test, when specimens are loaded with rising heat flux, the behavior

can change from cracking to a combination with brooming (see Fig. 6(a and b)). In these quasi-isotropic lay-ups, the tensile strength is dominated by the carbon fibres [50]. However, the tensile strength of the material can be affected before fibre degradation sets in, for example, when matrix depletion is present and thus the adhesion between fibre-matrix and plies is extremely weakened. As a result, the carbon fibres do not necessarily crack simultaneously during the tensile test, leading to failure of the specimen at lower forces [25]. Consequently, the fracture behavior of thermally damaged specimens contains information about the irradiation scenario. Thermal loads with low heat fluxes lead to comparatively homogeneous depth damage and thus single fracture types. In contrast, at high heat fluxes, combined fractures can occur due to the damage gradient until finally the entire specimen cross-section is completely damaged. In Table 1, the failure phenomena of all samples are summarized.

To characterize the mechanical properties of the uncoated and coated 8552/IM7 specimens after different thermal loading scenarios, the normalized (a, d) interlaminar shear strength τ/τ_0, (b, e) compressive strength $\sigma_c/\sigma_{c,0}$ and (c, f) tensile strength $\sigma_t/\sigma_{t,0}$ versus irradiation time t_l are shown in Fig. 7. Basically, the strength-time progression can be classified into three different ranges. These ranges are composed of negligible, beginning and extreme strength loss. For example, at $q = 5$ W/cm^2, the interlaminar shear strength hardly decreases until $t_l \leq 5$ s, between $5 < t_l < 17$ s the strength loss begins and from $t_l \geq 17$ s the strength collapses abruptly. The collapse occurs at a strength drop of approximately -20% and is reached at the lowest and highest heat flux in $t_l = 17 \pm 1.7$ and 1.3 ± 0.1 s, respectively. Below the -20% drop, the strength curve decreases approximately linearly. Thereby, at the lowest heat flux, the interlaminar shear strength per irradiation time drops by approximately $\tau / t_l = 3$ MPa/s and at the highest heat flux by even $\tau / t_l = 80$ MPa/s. Consequently, the irradiation time until this strength loss can be defined as the loading limit. Below this limit, the strength per time interval drops extremely, resulting in material collapse. Since the collapse of tensile and compressive strength is also noticeable from a -20% drop, loading limits can be introduced for all strength types (see -20% limits in Fig. 7).
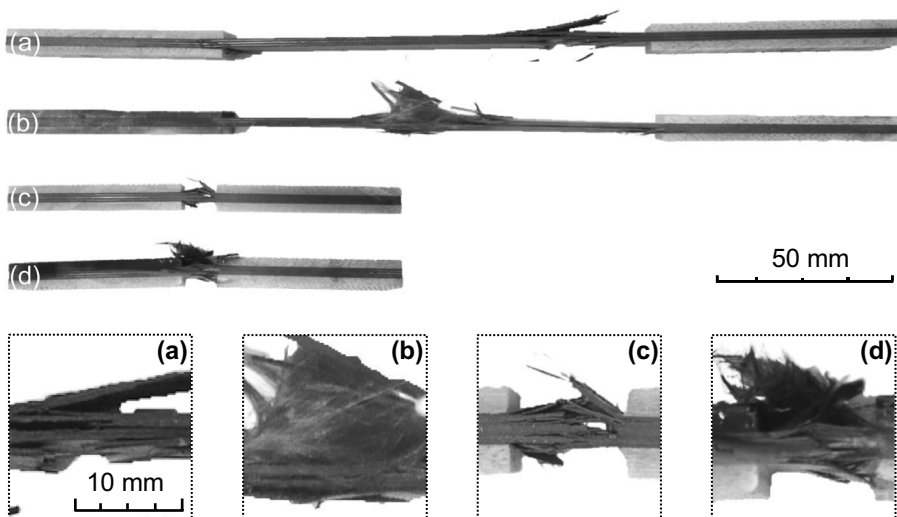

Fig. 6 Images of CFRP damage behaviour after: **a** $q = 5$ W/cm^2, $t_l = 5.0$ s and **b** $q = 50$ W/cm.^{2}, $t_l = 5.0$ s for tensile testing as well as **c** $q = 5$ W/cm^2, $t_l = 5.0$ s and **d** $q = 175$ W/cm^2, $t_l = 1.5$ s for compressive testing
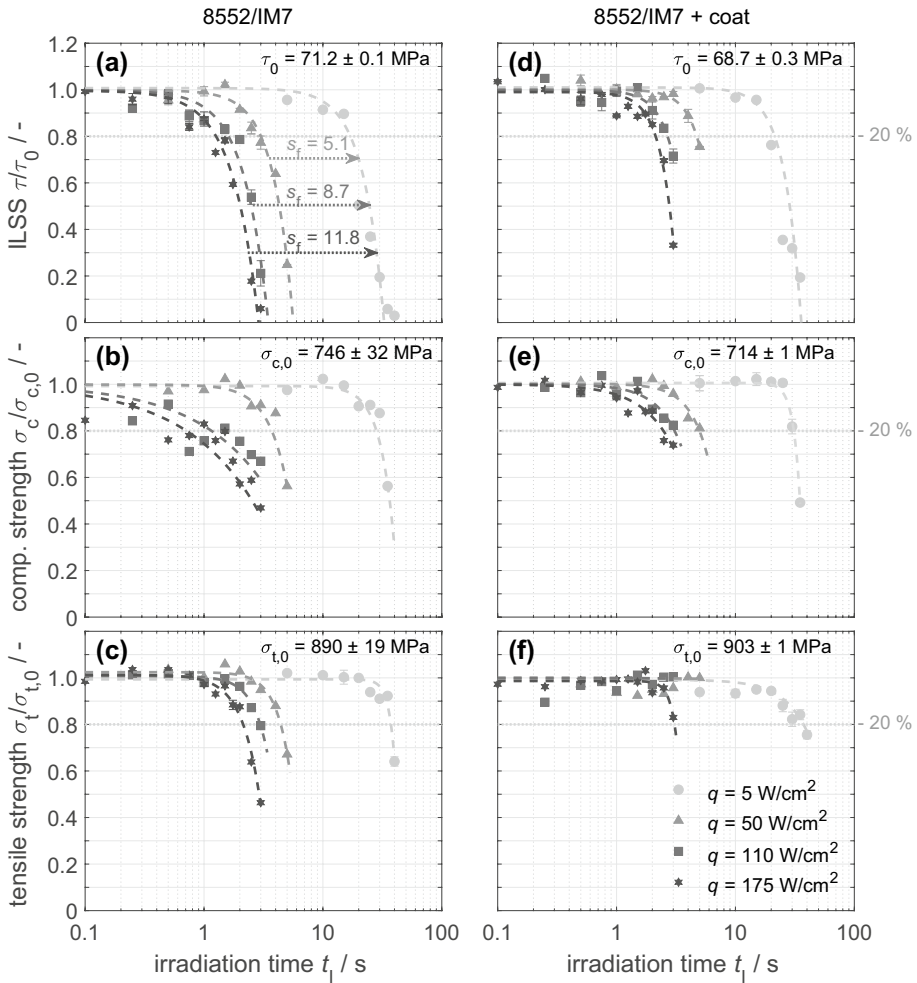
Fig. 7 Normalized interlaminar shear strength τ/τ_0, compressive strength $\sigma_c/\sigma_{c,0}$ and tensile strength $\sigma_t/\sigma_{t,0}$ **a–c** for 8552/IM7 as well as **d–f** for 8552/IM7 with coating against the irradiation time t_l. In addition, -20% strength losses and shift factors s_f are visualized

At high heat fluxes $q > 50$ W/cm^2, the strength drops only slightly until the material ignites. For example, at $q = 175$ W/cm^2 the material ignites in $t_l \geq 0.75$ s. Before ignition at $t_l = 0.5$ s, the residual normalized interlaminar shear strength changes to $\tau/\tau_0 = 0.97$, compressive strength to $\sigma_c/\sigma_{c,0} = 0.90$ and tensile strength to $\sigma_t/\sigma_{t,0} = 1.03$. As soon as ignition starts, the strength decreases significantly. Thus, the combustion of the specimen is a decisive damage criterion at high heat fluxes.

Furthermore, long-lasting low and short-lasting high heat fluxes affect the mechanical properties of coated and uncoated specimens differently. For example, for coated 8552/IM7 samples, the -20% interlaminar shear drop occurs delayed in $t_l = 21 \pm 2.1$ s at $q = 5$ W/cm^2 and in $t_l = 2.0 \pm 0.2$ s at $q = 175$ W/cm^2. This corresponds to a delay by a factor of $s_f = 21$ s / 17 s $= 1.2$ at the lowest and of $s_f = 1.5$ at the highest heat flux. Thus, the strength reduction can be delayed by the protective effect of a coating, especially at high heat

fluxes. In addition, the protective effect is also evident for compressive strength and tensile strength. The stiffness of the sample behaves similarly to the tensile strength. Once the tensile strength drops, the material also loses stiffness (see Table 1).

In Fig. 8, the time at -20% strength loss for (a) uncoated and (b) coated 8552/IM7 samples is plotted against heat flux q. This time not only decreases with rising heat flux, but also differs between strength types. For example, for uncoated specimens, the -20% strength loss occurs at $q = 5$ W/cm^2 for interlaminar shear strength in $t_{-20\%} = 17 \pm 1.7$ s, for compressive strength in $t_{-20\%} = 28 \pm 2.8$ s and for tensile strength in $t_{-20\%} = 40 \pm 4.0$ s. This sequence is existent because a slight and relatively homogeneous matrix degradation already appears after $t_1 = 15$ s along the sample cross-section. Due to this degradation, the fibre-matrix bonding as well as interlaminar adhesion of the plies is weakened, leading first to a reduction of the interlaminar shear strength. Only from $t_1 = 20$ s when delaminations appear, the compressive strength decreases, too. In comparison, tensile strength is affected last, because this strength type requires loss of fibre-matrix adhesion or degraded fibres. Thus, before delaminations occur, the strength of the material is only slightly affected.

However, above approximately $q > 75$ W/cm^2, the compressive strength is most sensitive to thermal loading. This change in sensitivity is due to the damage gradient in the thin specimens. For example, at $q = 175$ W/cm^2 and $t_1 = 0.5$ s, the matrix degradation extends to a depth of $z \sim 0.75$ mm and delaminations to $z \sim 0.25$ mm into the material. Since there is pronounced near-surface damage, the specimens tend to buckle during mechanical testing [54]. As a result, the compressive strength drops before the interlaminar shear strength.

In comparison, the coated specimens in Fig. 8(b) reach the 20% loss only at higher exposure times and with rising heat flux in unchanged sequence of strength types. Due to the protective effect of the coating, matrix degradation and especially the formation of delaminations can be delayed (see chapter 4.3). As a result, during compressive tests, buckling and brooming of the specimens occurs only at higher exposure times. Thus, a surface coating can prevent early material failure, especially under compressive loads.
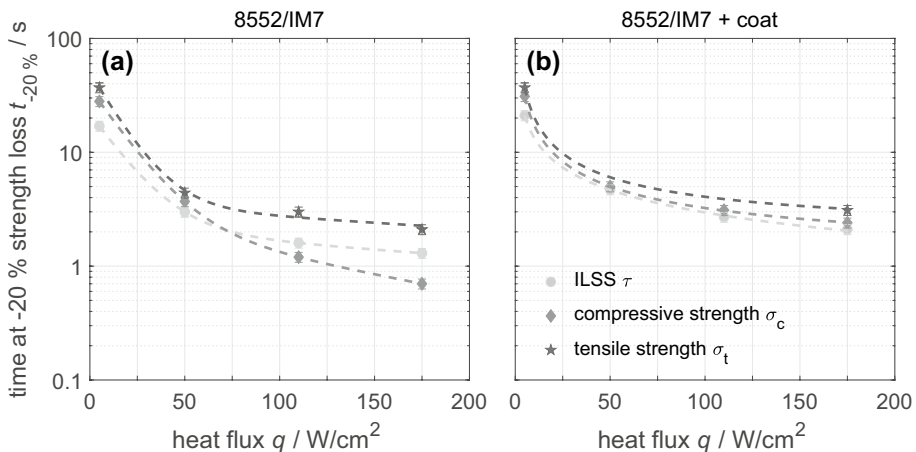

Fig. 8 Time $t_{-20\%}$ at -20% strength loss of interlaminar shear, compressive and tensile strength **a** for 8552/IM7 and **b** for 8552/IM7 with coating versus heat flux q

4.5 Prediction of Mechanical Properties

Under mechanical loading and defined temperature, polymeric material can have characteristic time dependent behavior [57]. Thus, the curve shape of the mechanical properties as a function of time does not change with rising temperature. These curves can be shifted horizontally with shift factors until a superposition with the reference curve at defined temperature occurs. Thereby, a master curve at given temperature is created, which can be utilized to predict curves at different temperatures using shift operations, based on the time–temperature superposition [57–59].

Similarly, superposition can be applied with strength-time curves to predict heat flux dependent mechanical properties. For this purpose, the irradiation times are shifted horizontally by multiplicative shift factors until the best superposition with the reference is achieved. The best superposition can be determined using the least squares method. Thereby, the shift factor is calculated, where the residual sum of squares between the shift and reference curve is minimal. For example, in Fig. 7(a), the irradiation times for the interlaminar shear strength values at $q = 50,110$ and 175 W/cm^2 are multiplied by shift factors of $s_f = 5.1$, 8.7 and 11.8 to obtain the minimum of the sum squares with the master curve from reference 8552/IM7 at $q = 5$ W/cm^2. Figure 9 shows the master curves for the normalized (a) interlaminar shear strength τ/τ_0, (b) compressive strength $\sigma_c/\sigma_{c,0}$ and (c) tensile strength $\sigma_t/\sigma_{t,0}$ of the 8552/IM7 with and without coating. Furthermore, the limits for 95% confidence level are given. In this time-heat flux superposition, irradiation times are shifted to the reference 8552/IM7 at $q = 5$ W/cm^2. An exception are the times for compressive strength values of the 8552/IM7 at $q \geq 110$ W/cm^2, because the superposition principle can only be applied for unchanged thermo-induced sensitivities of the strength types (see Fig. 8). Under this consideration, the master curves deviate from the interlaminar shear strength values by a root-mean square error RMSE of 4%, from compressive strength of 4% and from tensile strength of 4%. Thus, a high prediction quality is available.
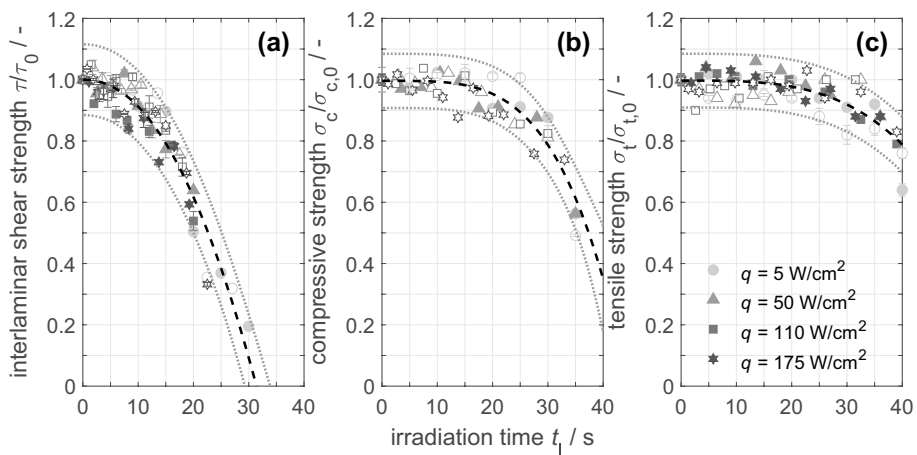

Fig. 9 Time-heat flux superposition for normalized **a** interlaminar shear strength τ/τ_0, **b** compressive strength $\sigma_c/\sigma_{c,0}$ and (**c**) tensile strength $\sigma_t/\sigma_{t,0}$ of 8552/IM7 with (filled symbols) and without coating (open symbols). The bounds reflect a 95% confidence interval. Reference is the 8552/IM7 at $q = 5$ W/cm^2 (shift factor $s_f = 1$)

Figure 10 summarizes the shift factors s_f as a function of heat flux q for (a) 8552/IM7 and (b) 8552/IM7 with coating. The reference is the 8552/IM7 at $q=5$ W/cm^2 with a shift factor of $s_f=1$. With rising heat flux, the shift factor increases for all strength types. Thereby, the shift factor represents the factor by which a material can be thermally loaded for a shorter time compared to the reference until a similar residual strength occurs. For example, the 8552/IM7 can be thermally loaded 11.8 times shorter at $q=175$ W/cm^2 than at $q=5$ W/cm^2 until a comparable residual interlaminar shear strength appears. If the residual interlaminar shear strength should be at least 80%, a maximum loading time of $t_{1,\ 5\ \text{W/cm}^2}=15\pm4$ s results at the lowest heat flux (see Fig. 9(a)). At $q=175$ W/cm^2, with a 95% probability, thermal irradiation must not exceed $t_{1,\ 175\ \text{W/cm}^2}=t_{1,\ 5\ \text{W/cm}^2}\ /\ s_f=1.3\pm0.3$ s. Furthermore, the loading limit at $q=50$ and 110 W/cm^2 of coated 8552/IM7 samples can be predicted (see Fig. 7(f)). According to the superposition, the -20% strength loss should occur for $t_{1,\ 50\ \text{W/cm}^2}=6.0\pm0.6$ s at $q=50$ W/cm^2 and for $t_{1,\ 110\ \text{W/cm}^2}=3.7\pm0.4$ s at $q=110$ W/cm^2. Thus, the predicted loading limits are consistent with the progression in Fig. 8(b).

In addition, strength-heat flux superposition can be used to predict residual strength at different heat fluxes. For example, the 8552/IM7 is thermally loaded at $q=175$ W/cm^2 for $t_{1,\ 175\ \text{W/cm}^2}=1.5$ s. This results in a shift factor of $s_f=11.8$ for interlaminar shear strength. Thereby, the loading time is equal to $t_{1,\ 5\ \text{W/cm}^2}=t_{1,\ 175\ \text{W/cm}^2}\cdot s_f=17.7$ s at $q=5$ W/cm^2. For this time, the master curve in Fig. 9(A) shows a residual strength of approximately $\tau/\tau_0=0.78$ or $\tau=55$ MPa, corresponding to the measured interlaminar shear strength of $\tau=56\pm1$ MPa. Consequently, time-heat flux superposition is a powerful tool that can be used to predict residual strength after both long-lasting low and short-lasting high heat fluxes.
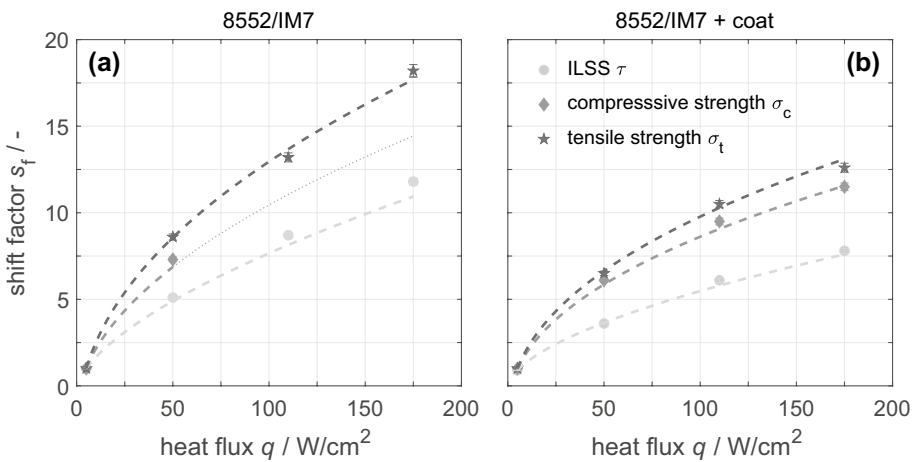

Fig. 10 Shift factors for interlaminar shear strength τ, compressive strength σ_c and tensile strength σ_t of **a** 8552/IM7 and **b** 8552/IM7 with coating. Reference is the 8552/IM7 at $q=5$ W/cm^2 (shift factor $s_f=1$)

5 Conclusion

In this study, the influence of different heat fluxes and exposure times on the thermal degradation of carbon fibre-reinforced polymers is investigated. Real scenarios are simulated, such as fully developed fires with long-lasting low heat fluxes and nuclear heat flashes with short-lasting high heat fluxes. For this purpose, coated and uncoated composites are thermally irradiated with heat fluxes between $q = 5 - 175$ W/cm^2 over a time period from $t_1 = 0.1$ to 40 s. For the thermal characterization of 8552/IM7, the temperature is recorded in different laminate depths and the samples are examined with non-destructive as well as destructive tests.

During thermal irradiation with low heat fluxes, less irradiation energy per time interval impinges on the sample surface. As a result, the material heats up slowly, resulting in small temperature gradients and relative homogeneous damage along the specimen cross-section. Thereby, the thermal degradation processes set in successively, beginning with the thermo-oxidation of the matrix near the surface, weakening of the fibre-matrix debonding, pronounced matrix degradation, formation of delaminations, matrix depletion and finally the decomposition of the fibres when the temperature is sufficiently high. During these processes, the mechanical strength drops significantly with the formation of delaminations, whereby first interlaminar shear, then compressive and finally tensile strength is affected.

In contrast, at high heat fluxes, the material heats up very quickly, leading to high temperatures and temperature gradients in the material. Thereby, ignition of the material, decomposition of the matrix and fibres as well as the formation of delaminations start almost simultaneously within seconds. An extreme damage gradient appears, dividing the cross-section generally into region with matrix depletion and regions with and without visible structural damage. As a result, the loss of mechanical properties, especially of thin specimens under compressive loading, occurs after short thermal exposures.

Once the residual strength is reduced by approximately -20%, the strength of the material collapses with rising exposure time. Thus, this threshold can be defined as the loading limit. Below this limit, the functionality of the material is no longer guaranteed. Furthermore, shift factors can be introduced using the strength-heat flux superposition. These shift factors indicate the factors by which a material can be thermally loaded for a shorter time compared to the reference until a similar residual strength result. In addition, mechanical properties can be predicted for both long-lasting low and short-lasting high heat fluxes with the limitation that this superposition only refers to the 2 mm thick 8552/IM7 with identical strength-time curve shapes.

However, to improve the safety of the carbon fibre-reinforced polymer application, it is advisable to coat the material. At low heat fluxes, the coating can be used as an early warning system against thermal damage due to the specific color change. In contrast, at high heat fluxes, the coating acts more as a protection of the underlying material due to the increased reflection of the impinging radiation and reduction of the temperature gradient along the sample cross-section.

Data availability The datasets generated during and/or analysed during the current study are available from the corresponding author on reasonable request.

References

1. Soutis, C.: Carbon fiber reinforced plastics in aircraft construction. Mater. Sci. Eng. A **412**, 171–176 (2005)
2. Clyne, T.W., Hull, D.: An Introduction to Composite Materials; 3rd ed.; Cambridge University Press, ISBN 9781139050586 (2019)
3. Sauer, M., Kühnel, M., Witten, E.: Report - Composites Market Report 2018 - Market developments, trends, outlook and challenges. Available online: www.carbon-connected.de (accessed on 7 Apr 2020).
4. Eurofighter Jagdflugzeug GmbH.: Technical Guide - Eurofighter Typhoon. Available online: www.eurofighter.com (accessed on 27 Apr 2020).
5. Neitzel, M., Breuer, U., Mitschang, P.: Handbuch Verbundwerkstoffe - Werkstoffe, Verarbeitung, Anwendung; 2nd ed.; Carl Hanser Verlag, ISBN 978–3446436961 (2014)
6. Azwa, Z.N., Yousif, B.F.: Characteristics of kenaf fibre / epoxy composites subjected to thermal degradation. Polym. Degrad. Stab. **98**, 2752–2759 (2013)
7. Naruse, T., Hattori, T., Miura, H., Takahashi, K.: Evaluation of thermal degradation of unidirectional CFRP rings. Compos. Struct. **52**, 533–538 (2001)
8. Ohno, S., Lee, M., Lin, K.Y., Ohuchi, F.S.: Thermal degradation of IM7/BMI5260 composite materials: characterization by X-ray photoelectron spectroscopy. Mater. Sci. Eng. A **293**, 88–94 (2000)
9. Ray, S., Ralph, P.: Handbook of Environmental Degradation of Materials; Third Edit.; Elsevier Inc., ISBN 9780323524728 (2018)
10. Trelles, J., Lattimer, B.Y.: Modelling thermal degradation of composite materials. Fire Mater. **31**, 147–171 (2007)
11. Schartel, B., Hull, T.R.: Development of fire-retarded materials — Interpretation of cone calorimeter data. Fire Mater. **31**, 327–354 (2007)
12. Mclean, A.D.: Burns and Military Clothing. J. R. Army Med. Corps **147**, 97–106 (2001)
13. Park, C., Zuo, J.: Advanced Hybrid Loop Technology for High Heat Flux Laser Cooling.; 3rd International Energy Conversion Engineering Conference (2005)
14. Larrimbe, L., Pettin, M., Nikbin, K., Jones, E.L., Katz, A.P., Christopher, J., Decerbo, J., Brown, P., Vandeperre, L.J.: High Heat Flux Laser Testing of HfB 2 Cylinders. J. Am. Ceram. Soc. **100**, 293–303 (2017)
15. Howell, J.R., Pinar Mengüç, M.: Thermal Radiation Heat Transfer; 6th ed.; Taylor & Francis Inc., ISBN 978–1466593268 (2016)
16. Lattimer B.Y., Ouellette J., Trelles J., Associates, H.: Thermal Response of Composite Materials to Elevated Temperatures. Fire Technol. **47**, 823–850 (2011)
17. Lattimer, B.Y., Ouellette, J.: Properties of composite materials for thermal analysis involving fires. Compos. Part A Appl. Sci. Manuf. **37**, 1068–1081 (2006)
18. Mouritz, A.P., Feih, S., Kandare, E., Mathys, Z., Gibson, A.G., Jardin, P.E. Des, Case, S.W., Lattimer, B.Y.: Review of fire structural modelling of polymer composites. Compos. Part A **40**, 1800–1814 (2009)
19. Eibl, S.: Quantification of a thermal pre-load on polymer matrix composites by the degradation and colour change of polyurethane top coats. Mater. Sci. Eng. Technol. **47**, 388–399 (2016)
20. Eibl, S., Wolfrum, J.: Prospects to separately estimate temperature and duration of a thermal pre-load on a polymer matrix composite. J. Compos. Mater. **47**, 3011–3025 (2012)
21. Dao, D.Q., Luche, J., Richard, F., Rogaume, T., Bourhy-Weber, C., Ruban, S.: Determination of characteristic parameters for the thermal decomposition of epoxy resin / carbon fibre composites in cone calorimeter. Int. J. Hydrogen Energy 1–12 (2012)
22. Rallini, M., Natali, M., Kenny, J.M., Torre, L.: Effect of boron carbide nanoparticles on the fire reaction and fire resistance of carbon fiber/epoxy composites. Polymer (Guildf). **54**, 5154–5165 (2013)

23. Mouritz, A.P., Mathys, Z., Gibson, A.G.: Heat release of polymer composites in fire. Compos. Part A Appl. Sci. Manuf. **37**, 1040–1054 (2006)
24. Eibl, S.: Influence of carbon fibre orientation on reaction-to-fire properties of polymer matrix composites. Fire Mater. **36**, 309–324 (2012)
25. Vetter, T., Bibinger, J., Zimmer, F., Eibl, S., Gudladt, H.-J.: Characterization of one-sided thermal damage of carbon fiber reinforced polymers by means of depth profiles. J. Compos. Mater. **54**, 3699–3713 (2020)
26. Eibl, S.: Potential for the formation of respirable fibers in carbon fiber reinforced plastic materials after combustion. Fire Mater. **41**, 808–816 (2017)
27. Meilunas, R.J., Bentsen, J.G., Steinberg, A.: Analysis of aged paint binders by FTIR spectroscopy. Stud. Conserv. **35**, 33–51 (1990)
28. Hexcel Composites.: Datasheet - HexPly® 8552, Epoxy matrix (180 °C / 356 °F curing matrix). Available online: www.hexcel.com (accessed on 12 May 2020).
29. Eibl, S.: Observing Inhomogeneity of Plastic Components in Carbon Fiber Reinforced Polymer Materials by ATR-FTIR Spectroscopy in the Micrometer Scale. J. Compos. Mater. **42**, 1231–1246 (2008)
30. Mankiewicz Gebr. & Co. Datasheet - SEEVENAX® primer 113–24 Available online: www.datasheets. mankiewicz.com (accessed on 30 Apr 2020).
31. Mankiewicz Gebr. & Co. Datasheet - ALEXIT® Top coat 472–22. Available online: www.datasheets. mankiewicz.com (accessed on 30 Apr 2020).
32. DELO Industrie Klebstoffe GmbH. Datasheet - DELO-DUPOX® 1895. Available online: www. hillmann-geitz.de (accessed on 2 May 2020).
33. Morgen, J.H.: SFPE Handbook of Fire Protection Engineering; 5th ed.; Springer New York Heidelberg, ISBN 9781493925643 (2016)
34. Wenig, P.: Steuerung und Charakterisierung von leistungsstarken Lichtquellen zur Materialerprobung - Doctoral thesis. Univ. Fed, Armed Forces Hambg (2012)
35. Pedrotti, F., Pedrotti, L., Bausch, W., Schmidt, H.: Optik für Ingenieure; 4th ed.; Springer Berlin Heidelberg, ISBN 3540228136 (2008)
36. InfraTec GmbH.: User manual - VarioCAM high resolution. Available online: www.infratec.de (accessed on 23 Apr 2020).
37. IEC 60584–1:2013 Thermocouples - Part 1: EMF specifications and tolerances; English version. VDE Verlag (2013)
38. Sobulska, M.; Zbicinski, I. *Flame Spray Drying: Equipment, Mechanism, and Perspectives*; 1st ed.; CRC Press, 2021; ISBN 9780367569310.
39. Robitaille, P.-M.: Kirchhoff's Law of Thermal Emission: 150 Years. **4**, ISBN 1555–5534 (2009)
40. Elhajjar, R., Grant, P., Ashforth, C.: Composite Structures: Effects of Defects; 1st ed.; JohnWiley & Sons Ltd, ISBN 978–1–118–99772–7 (2018)
41. DIN EN ISO 16810 Non-destructive testing - Ultrasonic testing; German version. Beuth Verlag Berlin (2014)
42. DIN EN 2563 Carbon fibre reinforced plastics - Unidirectional laminates - Determination of the apparent interlaminar shear strength; German version. Beuth Verlag Berlin (1997)
43. DIN EN ISO 527–4 Determination of tensile properties - Part 4: Test conditions for isotropic and orthotropic fibre-reinforced plastic composites; German version. Beuth Verlag Berlin (1997)
44. DIN EN ISO 14126 Fibre reinforced plastic composites - Determination of compressive properties in the in-plane direction; German version. Beuth Verlag Berlin (2000)
45. Von Böckh, P., Stripf, M.: Technische Thermodynamik; 2nd ed.; Springer Vieweg, ISBN 978–3–662–46889–0 (2015)
46. Eibl, S.: Reliable and universally applicable chemometric techniques based on infrared spectroscopy to non-destructively quantify thermal damage of carbon fibre reinforced epoxy matrix composites. Polym. Test. **76**, 396–410 (2019)
47. Dao, B., Hodgkin, J., Krstina, J., Mardel, J., Tian, W.: Accelerated Aging Versus Realistic Aging in Aerospace Composite Materials . II. Chemistry of Thermal Aging in a Structural Composite. J. Appl. Polym. Sci. **102**, 3221–3232 (2006)
48. Huang, J., Yang, H., Chen, M., Ji, T., Hou, Z., Wu, M.: An infrared spectroscopy study of PES PVP blend and PES-g-PVP copolymer. Polym. Test. **59**, 212–219 (2017)
49. Marshall, P., Price, J.: Topography of carbon fibre surfaces. Composites **22**, 388–393 (1991)
50. Hexcel Corporation. Datasheet - HexTow® IM7 Carbon Fiber. Available online: www.hexcel.com (accessed on 9 Apr 2020).
51. Eibl, S.: Influence of unwoven roving and woven fabric carbon fiber reinforcements on reaction-to-fire properties of polymer matrix composites. Fire Mater. **44**, 557–572 (2020)

52. Mouritz, A.P., Gibson, A.G.: Fire Properties of Polymer Composite Materials; Springer Netherlands **53**, ISBN 978–1–4020–5355–9 (2012)

53. Wolfrum, J., Eibl, S., Lietch, L.: Rapid evaluation of long-term thermal degradation of carbon fibre epoxy composites. Compos. Sci. Technol. **69**, 523–530 (2009)

54. Grellmann, W., Seidler, S.: Polymer Testing; 2nd ed.; Carl Hanser Verlag, ISBN 9781569905487 (2013)

55. Schürmann, H.: Konstruieren mit Faser-Kunststoff-Verbunden; 2nd ed.; Springer Berlin Heidelberg, 2007; ISBN 9783540721895 (2007)

56. Ehrenstein, G.W.: Faserverbund-Kunststoffe; 2nd ed.; Carl Hanser Verlag, ISBN 978–3446227163 (2006)

57. Gillen, K.T., Bernstein, R., Celina, M.: Challenges of accelerated aging techniques for elastomer lifetime predictions. Rubber Chem. Technol. **88**, 1–27 (2015)

58. Nakada, M., Miyano, Y., Kinoshita, M.: Time-temperature dependence of tensile strength of unidirectional CFRP. J. Compos. Mater. **36**, 2567–2581 (2002)

59. Krauklis, A.E., Akulichev, A.G., Gagani, A.I., Echtermeyer, A.T.: Time-temperature-plasticization superposition principle: Predicting creep of a plasticized epoxy. Polymers (Basel). **11**, 1848 (2019)

Publisher's Note Springer Nature remains neutral with regard to jurisdictional claims in published maps and institutional affiliations.